Journal of Turbulence

ISSN: (Print) (Online) Journal homepage: https://www.tandfonline.com/loi/tjot20

Transitional and turbulent flows in rectangular ducts: budgets and projection in principal mean strain axes

Paolo Orlandi & Sergio Pirozzoli

To cite this article: Paolo Orlandi & Sergio Pirozzoli (2020): Transitional and turbulent flows in rectangular ducts: budgets and projection in principal mean strain axes, Journal of Turbulence, DOI: 10.1080/14685248.2020.1779276

To link to this article: https://doi.org/10.1080/14685248.2020.1779276

Published online: 18 Jun 2020.

JOURNAL OF TURBULENCE
https://doi.org/10.1080/14685248.2020.1779276

Taylor & Francis
Taylor & Francis Group

Transitional and turbulent flows in rectangular ducts: budgets and projection in principal mean strain axes

Paolo Orlandi and Sergio Pirozzoli

Dipartimento di Ingegneria Meccanica e Aerospaziale, Università La Sapienza, Roma, Italy

ABSTRACT

We carry out Direct Numerical Simulation (DNS) of flows in closed rectangular ducts with several aspect ratios. The Navier–Stokes equations are discretised through a second-order finite difference scheme, with non-uniform grids in two directions. The duct cross-sectional area is maintained constant as well as the flow rate, which allows to investigate which is the appropriate length scale in the Reynolds number for a good scaling in the laminar and in the fully turbulent regimes. We find that the Reynolds number based on the half length of the short side leads to a critical Reynolds number which is independent on the aspect ratio (A_R), for ducts with $A_R > 1$. The mean and rms wall-normal velocity profiles are found to scale with the local value of the friction velocity. At high friction Reynolds numbers, the Reynolds number dependence is similar to that in turbulent plane channels, hence flows in rectangular ducts allow to investigate the Reynolds number dependency through a reduced number of simulations. At low Re, the profiles of the statistics differ from those in the two-dimensional channel due to the interaction of flow structures of different size. The projection of the velocity vector and of the Reynolds stress tensor along the eigenvectors of the strain-rate tensor yields reduced Reynolds stress anisotropy and simple turbulence kinetic energy budgets. We further show that the isotropic rate of dissipation is more difficult to model than the full dissipation rate, whose distribution does not largely differ from that of turbulence kinetic energy production. We expect that this information may be exploited for the development of advanced RANS models for complex flows.

ARTICLE HISTORY
Received 8 January 2020
Accepted 11 May 2020

KEYWORDS
Direct Numerical Simulation; rectangular ducts; transition; wall turbulence

1. Introduction

Many efforts have been directed to understanding laminar, transitional and turbulent flows near walls. The turbulent channel has been largely considered in Direct Numerical Simulations (DNS), where two homogeneous directions allow to get satisfactory statistics profiles with a limited number of fields. This flow cannot be exactly reproduced in laboratory experiments where the effects of the lateral walls cannot be eliminated. Several studies, for instance the most recent by Vinuesa et al. [1] and Vinuesa et al. [2], were

CONTACT Paolo Orlandi paolo.orlandi@uniroma1.it Dipartimento di Ingegneria Meccanica e Aerospaziale, Università La Sapienza, Via Eudossiana 16, I-00184 Roma, Italy

devoted to investigating differences between ideal two-dimensional turbulent channels and rectangular ducts with high and low aspect ratios. The simulations and the experiments were performed at intermediate Reynolds number ($Re_\tau \approx 500$). The transitional regime for the square duct was considered numerically by Uhlmann et al. [3] and experimentally by Owolabi et al. [4]. Numerically it is easy to relate the friction $Re_\tau = u_\tau L/\nu$, with L the length of the side of the square duct and u_τ the mean friction velocity, to the bulk Reynolds number $Re_L = U_b L/\nu$. They found that the turbulent regime is observed above $Re_L = 1077$, and up to $Re_L = 2000$ there is a linear relationship between the two Reynolds numbers. The value $Re_L = 1077$ does not differ too much from that in circular pipes ($Re_C = 1125$ by [5]) and in a plane channel ($Re_C = 1000$ by [6]). Orlandi et al. [7] through DNS of Poiseuille and Couette flows observed a jump on the total turbulence kinetic energy respectively at $Re \approx 1800$ for Poiseuille and $Re = 1000$ for the Couette flows. These Reynolds numbers are defined as $Re = U_M H/\nu$ with H half channel width and U_M the maximum of the laminar parabolic Poiseille profile and the wall velocity for Couette. It is important to recall that the initial amplitude of disturbances in numerical experiments or the inlet conditions in laboratory experiments can affect the value of the critical Reynolds. The sensitivity to the disturbances was carefully investigated by Fitzgerald [8] reporting the results of sophisticated experiments in circular pipes [9], showing that reduction of the amplitude of the disturbance may lead to an increase of the transition Reynolds number up to $Re = 18,000$, much greater than the value obtained by Reynolds [10]. Orlandi [11] performed numerical experiments to further analyse the influence of the initial disturbances in circular pipes. From the observation that there are no large differences in the critical Reynolds number between flows with well-localised secondary flows and flows without it (circular pipe and plane channel) it is worth analysing also in rectangular ducts which is the appropriate length scale giving a fixed transition Reynolds number, or whether a dependence on the aspect ratio exists. Tatsumi and Yoshimura [12] performed a linear stability analysis observing that the flow is stable for any aspect ratio $A_R > 3.2$. On the other hand, DNS by Takeishi et al. [13] has shown that the transition Reynolds number slightly depends on A_R for $A_R < 5$, and it becomes constant at higher A_R. An effect of the initial conditions is apparent in those studies, hence in the present simulations we have decided to assign initial velocity distributions different from realistic conditions. The influence of the initial conditions explains why a section is here dedicated to analyse the trend towards statistically steady conditions.

In non-circular ducts, several length scales can be defined. One largely used is the hydraulic diameter $D_h = 4A/P$, with P the perimeter and A the cross-section area of the duct ($Re_D = U_b D_h/\nu$). In the present simulations, the reference length is assumed to be the radius of an equivalent pipe, r_p ($A = \pi r_p^2$), hence the relevant computational Reynolds number is $Re = U_b r_p/\nu$. This choice fixes $A = \pi$, which is maintained for all cases. A further length scale can be taken to be the length of either the short or long sides of the duct, here respectively denoted as L_3 and $L_2 (= A_R L_3)$, related through $L_2 L_3 = \pi$. The former has greater relevance in rectangular ducts, as it becomes the channel height in the limit of infinite aspect ratio. As a first check of the differences in the profiles of the friction factor $C_f = 2u_\tau^2/U_b^2$ versus the three Reynolds numbers above reported can be obtained by using equation (3-48) at p.113 of White [14]. The analytical linear profiles, confirmed by the present simulations, allow to see different trends of C_f with the Reynolds numbers, and good collapse of the linear profiles with Re_3, namely the Reynolds number based on

the shorter side half-length ($L_3/2$). Takeishi et al. [13] also adopted $L_3/2$ as the reference length to evaluate the transitional Reynolds number. Simulations at higher Reynolds number show that after the critical one good collapse of the friction coefficient with the duct aspect ratio is found, regardless of the length scale used in the definition of *Re*.

The secondary motions, widely analysed in several DNS papers, starting from [15] at low Re, and ending with [16] at much higher Re, is rather weak with respect to the main motion, hence it is likely that they do not alter substantially the statistical profiles with respect to canonical wall-bounded flows. In particular, this should be the case at high values of the Reynolds numbers, at which the strongest streamwise vorticity becomes localised in a smaller and smaller region [16]. Secondary motions have been deeply investigated by Joung et al. [17], and a clear picture of its effect can be observed in their figure 6 reporting undulations of $\tau_w/\overline{\tau_w}$ near the corner, with differences among the profiles at different Reynolds numbers. The reduction of friction approaching the corner should also appear on the shape and size of the streamwise vortical structures, and therefore on the distribution of the turbulence kinetic energy. The decrease of the wall shear stress should be different along the short and long sides of the rectangular duct. The present simulations are focused to investigate the variations with the Reynolds number and with the aspect ratio of several statistics in particular to demonstrate whether the wall scaling with the averaged or the local friction velocity hold. In the corners the local Re_τ decreases, and therefore, in the same flow it is possible to investigate whether the Reynolds number dependence of the statistics in wall units shown by Orlandi et al. [7] for the plane channel is also recovered.

Projection of the velocity vector and of the Reynolds stress tensor along the eigenvectors of the strain-rate tensor yields reduced Reynolds stress anisotropy, and simpler turbulence kinetic energy budgets. We further show that the isotropic rate of dissipation is more difficult to model than the full dissipation rate, whose distribution does not largely differ from that of turbulence kinetic energy production. We expect that this information may be exploited for the development of advanced RANS models for complex flows. Often the budgets of turbulence kinetic energy are evaluated through converged statistics. However, turbulence kinetic energy budget evaluated during the initial transient reveals that far from equilibrium local variations of the turbulence kinetic energy are strictly related to those of the convective term, with much activity in the bulk flow. On the other hand, under statistically steady conditions the effect of the convective terms is reduced, and all the activity tends to be concentrated near the walls

The mean and rms wall-normal velocity profiles are found to scale with the local value of the friction velocity. At high friction Reynolds numbers, the Reynolds number dependence is similar to that in turbulent plane channels, hence flows in rectangular ducts allow to investigate the Reynolds number dependency through a reduced number of simulations. At low Re, the profiles of the statistics differ from those in the two-dimensional channel due to the interaction of flow structures of different size.

In plane channel, DNS are often performed by pseudospectral methods, similar or equal to that described in [18]. These results can be considered as reference solutions to validate those obtained by other numerical methods. However, Bernardini et al. [19] demonstrated that by using the same resolution the streamwise spectra by second-order schemes were as good as those by pseudospectral methods in a convecting reference frame.

However, in the steady reference frame the profiles of the statistics did not show any appreciable difference with those by pseudospectral methods. The improvement achieved

in the convective reference frame was detected in the streamwise velocity spectra, at high wavenumber with low energy content. Based on these observations, in the present study a second-order staggered finite-difference scheme is used, with the further advantage of using non-uniform grids in two space directions, adapted from a code previously developed for the simulations of Poiseuille and Couette flows.

Another possible alternative is the use of compressible flow solvers adapted for low-Mach-number flows [16], which were shown to yield nearly identical solutions as incompressible solvers.

2. Flows set-up

A large number of flow cases have been simulated, with resolution depending on the Reynolds number. At low and intermediate Re the computational mesh used is $161 \times 161 \times 161$, up to $513 \times 385 \times 257$, respectively in the streamwise x_1, lateral x_2 and vertical x_3 directions. The smaller number of points in x_3 than those in x_2 is due to the reduction of L_3 with the increase of the aspect ratio A_R. In the present simulations, the flow rate is maintained constant by adding at each time step a mean pressure gradient Π balancing the friction losses due to the walls. In the evaluation of the flow rate, the cross-sectional area appears which has been maintained constant. At each Re, several A_R were considered, namely 1, 2, 4, 5, 6, 7. Simulations with $A_R = 1.5$ were also performed in a range of Re close to the critical one. For the governing equations, the reader may refer to Orlandi [20, Chapter 9], with no-slip boundary conditions imposed at the duct walls.

The same procedure of low-storage Runge–Kutta time integration of the nonlinear terms, and implicit treatment of the viscous terms was also used. The fundamental difference from the method developed for flows with two homogeneous directions (spanwise and streamwise) resides in the solution of the elliptical equation. In the case of two homogeneous direction, the use of two Fast Fourier Transforms (FFT) and a tridiagonal solver (see [20, Chapter 9]) allows to numerically solve Poisson equation within round-off errors. In order to get a fast solution at high Reynolds numbers, a large number of processors can be used through the MPI (Message Parallel Interface) directives, by subdividing the computational domain into pencil-shaped sub-domains. In the presence of two directions with grid non-uniformity, the Poisson equation can be solved either through a multigrid method [17], or direct solvers based on the cyclic reduction algorithm as FISHPACK, developed at NCAR by Adams et al. [21]. The convergence of multigrid algorithms is strongly connected to coordinate stretching, which sets the eigenvalues of the associated matrices. Hence, to avoid possible slow convergence, the FISHPACK subroutine is a good choice, clearly less efficient than FFT-based direct solvers. The main disadvantage of the FISHPACK consists in a limitation of the number of processors, since the computational domain can only be divided into slabs along the streamwise direction.

The initial distribution of the streamwise velocity is irrelevant to establish the flow statistics at the final steady state. However, it is mandatory that $U_b = \iiint u_1 \, \mathrm{d}x_1 \, \mathrm{d}x_2 \, \mathrm{d}x_3/(L_1 L_2 L_3) = 1$. To be more precise our initial streamwise velocity is

$$u_1(x_2, x_3) = C(H - d) \quad d = (H - |x_2|)^2 + (H - |x_3|))^2 \quad \text{for } d < H \tag{1}$$

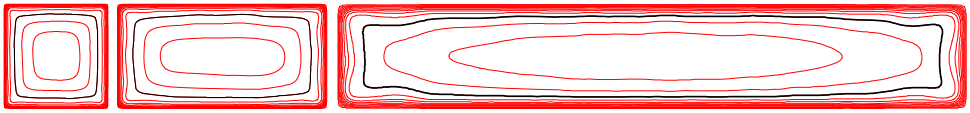

Figure 1. Contours of mean streamwise velocity $< U_1(x_2, x_3) >$ for DNS of ducts at $Re = 5000$, for (a) $A_R = 1$, (b) $A_R = 2$, (c) $A_R = 6$, in increments $\Delta = 0.1U_b$, the black line is $\langle U_1(x_2, x_3)\rangle = U_b$.

($H = L_2/2$) and $u_1 = 0$ elsewhere. Random disturbances are added, hence the other two velocity components are obtained from the divergence-free condition. The constant C is such that $U_b = 1$. This distribution is concentrated at the centre of the duct, and velocity is very small near the vertical walls.

We have found that within two time units the field adjusts by conforming to the shape of the duct. Previous DNS [3] showed that for square ducts and for $L_1/(0.5L_3) > 10$, the mean wall shear stress does not change. In the present simulations for all A_R, we use $L_1/r_p = 16$, hence at $A_R = 1$ we have $L_1/(0.5L_3) = 18.05$. For high A_R, L_3 decreases and since, as later on shown, L_3 is the relevant length scale, the duct is long enough to resolve the energy-containing longitudinal structures. This streamwise length is satisfactory at intermediate values of Re, but not enough at Re close to the critical value, at which localised turbulent structures may form as those see in flow visualisations in domains three times longer than the present one [13].

Depending on A_R and on the value of Re the simulations evolve for a different time. At high Reynolds number, the transient time to reach the instant at which Π oscillates around the averaged $\overline{\Pi}$ is short. However, the simulations must evolve for a sufficient time in order to have distributions of the statistics in the $x_2 - x_3$ planes respecting as much as possible the geometrical symmetries. At low Re, and, in particular, under laminar conditions a long initial transient is necessary to damp the initial disturbances through viscous diffusion. The averaged wall shear stress $\overline{\tau_w}$, calculated through $\overline{\tau_w} = \overline{\Pi} L_2 L_3/(L_2 + L_3)$, allows to define the averaged friction velocity $\overline{u_\tau} = \sqrt{\overline{\tau_w}}$, and the friction coefficient, $C_f = 2\overline{\tau_w}/U_b^2$.

The shapes of the duct sections are depicted in Figure 1 through contour plots of the mean streamwise velocity component at $Re = 5000$. The plots are shown only for $A_R = 1, 2, 6$ to appreciate how L_3 reduces and L_2 increases. Although the simulations have been carried out with constant duct area, in the figure we keep the same L_3 for greater clarity. The mean quantities, here indicated with capital letters, are evaluated by averaging in the streamwise direction x_1 of the duct, and in time. The averages in time were estimated by storing a sufficient number of fields saved every 1.0 time units. It may be argued that to reproduce the expected geometrical symmetries a huge number of realisations are necessary, however, Figure 1 shows that a rather good distribution is achieved by the number N in Table 1. Higher-order statistics may require an even greater number of samples, hence further averaging is carried out by quarters of the cross section. This is similar to what done in plane channels, in which statistics are averaged between the two walls.

A list of the global results for the flow cases herein simulated and the corresponding mesh properties is given in Table 1.

Table 1. List of parameters for the turbulent cases, the first number after A indicates A_R, the subscript indicates the Re number given in the first column. N_f is the number of fields used to evaluate the statistics. N_x, N_y, N_z are the number of grid points in the axial, in the wider lateral direction and in the shorter vertical direction. The area is fixed and equal to π. The total friction is indicated by Π and the contribution of the longer side is τ_2. Re_D is the Reynolds number based on the hydraulic diameter, and Re_3 is the Reynolds number scaled with the shorter side half-length ($L_3/2$).

Flow case	Re	Re_τ	N_f	N_x	N_y	N_z	$\overline{\tau_2}/\overline{\Pi}$	$10\overline{\Pi}$	Re_D	Re_3
$A1_{2K}$	2500	172	969	193	193	193	0.50	0.338	2500	2216
$A2_{2K}$	2500	172	701	193	193	193	0.69	0.358	2357	1567
$A5_{2K}$	2500	177	701	193	193	193	0.87	0.480	1863	991
$A7_{2K}$	2500	162	701	193	193	193	0.92	0.451	1654	837
$A1_{5K}$	5000	323	939	257	257	193	0.50	0.295	5000	4431
$A2_{5K}$	5000	328	528	257	257	193	0.69	0.323	4714	3133
$A5_{5K}$	5000	340	475	257	257	193	0.87	0.440	3727	1982
$A7_{5K}$	5000	342	418	257	257	193	0.91	0.501	3307	1675
$A1_{7K}$	7750	474	694	385	257	193	0.50	0.266	7750	6868
$A2_{7K}$	7750	481	411	385	257	193	0.69	0.290	7307	4856
$A5_{7K}$	7750	503	359	385	257	193	0.87	0.400	5777	3071
$A7_{7K}$	7750	509	283	385	257	193	0.90	0.463	5126	2596
$A1_{15K}$	15,000	859	305	513	385	257	0.50	0.232	15,000	13,293
$A2_{15K}$	15,000	872	141	513	385	257	0.69	0.254	14,140	9400
$A5_{15K}$	15,000	915	121	513	385	257	0.87	0.353	11,180	5945
$A7_{15K}$	15,000	927	118	513	385	257	0.91	0.409	9922	5024

3. Results

3.1. Path to the steady-state regime

There could be different views on the tendency towards the statistical steady state at low and high Reynolds numbers, depending on the initial conditions. In the present simulations, large disturbances at both large and small scales are imposed at $t = 0$, resulting in large turbulence kinetic energy and friction. The disturbances are damped at a different rate, depending on viscosity, and in particular friction initially decays. At a certain time, which is a function of duct shape and Reynolds number, all flow scales have little energy remaining. At Reynolds numbers lower than the critical one then disturbances keep decaying, eventually leading to a laminar state. At Re higher than the critical value, the strength of the structures instead grows exponentially for a short time, and a peak of the pressure gradient is reached, at which near-wall structures of the 'right' size form, as typical of wall-bounded flows. Animations of the instantaneous vorticity fields averaged in the streamwise directions [22] describe this process quite well. A global view of the complex flow dynamics may be drawn from the time evolution of Π in the early stages of evolution, reported at $Re = 2500$ in Figure 2(a) and at $Re = 7750$ in Figure 2(c).The corresponding time evolutions in the last 300 time units, after a statistical steady state is reached, are given in Figure 2(b) and 2(d), respectively. The observed oscillations of Π for certain values of A_R are typical of marginally turbulent flows, which are entirely suppressed for $A_R = 7$ and $Re = 2500$, as expected in the laminar regime. At high Reynolds number, the long-time evolution of Π shows that amplitude and frequency of the oscillations do not change with the aspect ratio, whereas flow resistance increases with A_R. Figure 2(c) shows that at $Re = 2500$ the initial velocity field yields larger resistance the higher is A_R. In a few time units Π rapidly reaches a minimum, which is then followed by a short time interval with sharp growth of Π, which is steeper the higher is A_R, and a relative maximum is

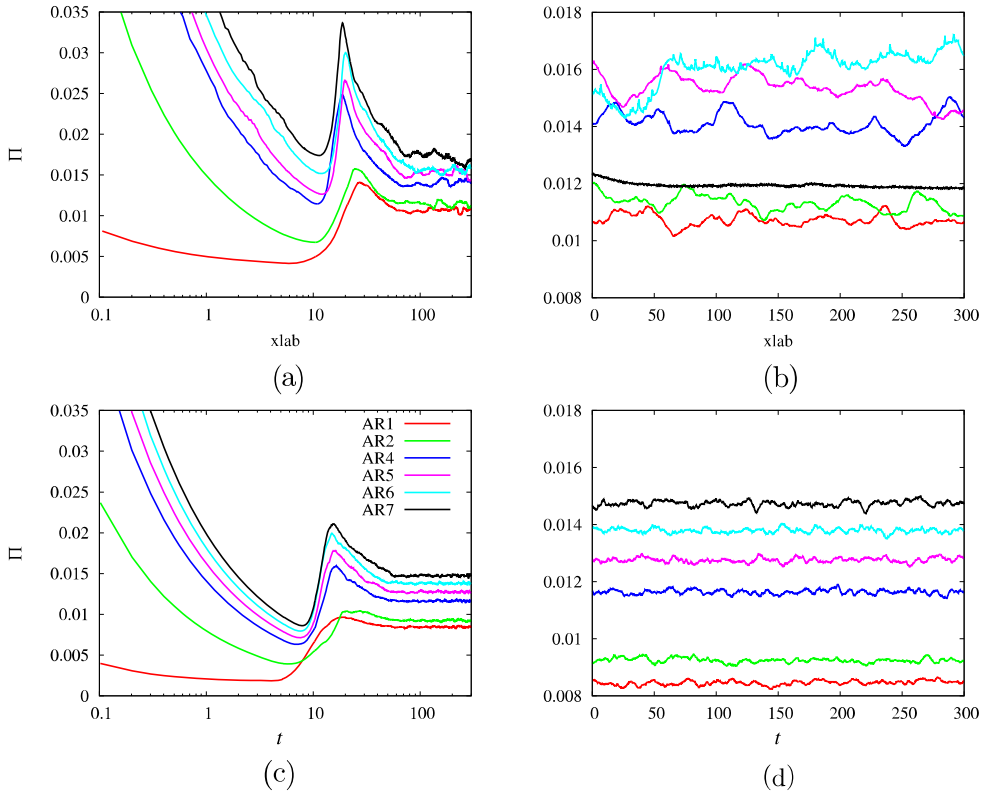

Figure 2. Time evolution of mean pressure gradient: (a) and (c) with time axis in log scale to emphasise the initial stages of transition to turbulence; (b) and (d) with time axis in linear scale, to focus on the last 300 time units and emphasise frequency and amplitude of the excursions. Data at $Re = 2500$ are shown in (a) and (b), and at $Re = 7750$ in (c) and (d). Aspect ratios are shown in panel (c).

reached. The subsequent decay yields a state in which Π oscillates around a mean value. At $Re = 2500$ the evolution is similar, but a laminar condition is reached for $A_R = 7$ (black line in Figure 2 b). This figure further shows that the large scales near the walls induce low-frequency, large-amplitude excursions of Π. When A_R is reduced, the frequency increases and the amplitude decreases.

In wall-bounded flows, there is a close connection between friction and turbulence kinetic energy. In fact, the highest levels of turbulence kinetic energy are located near the wall, where it is produced by interaction of the mean shear with the turbulent stresses. The equation for the time evolution of the turbulence kinetic energy $q = \overline{u_i u_i}/2$ over the duct cross-section (here the overline indicates averages in the periodic streamwise direction) describes the complex mechanisms of production, dissipation and transfer from one to another region [23, p.315]

$$\frac{\partial q}{\partial t} = \underbrace{-\frac{1}{2}\overline{U_k}\frac{\partial \overline{u_i u_i}}{\partial x_k}}_{C_K} \underbrace{-\frac{1}{2}\frac{\partial \overline{u_i u_i u_k}}{\partial x_k} + \overline{u_i \frac{\partial p}{\partial x_i}}}_{T_K} + \underbrace{\frac{1}{Re}\overline{u_i \nabla^2 u_i}}_{D_K} \underbrace{-\overline{u_i u_k}\frac{\partial \overline{U_i}}{\partial x_k}}_{P_K}. \tag{2}$$

The correlations between velocity fluctuations (indicated in small letters in this equation) contribute to the evolution of turbulence kinetic energy, and velocity fluctuations yield

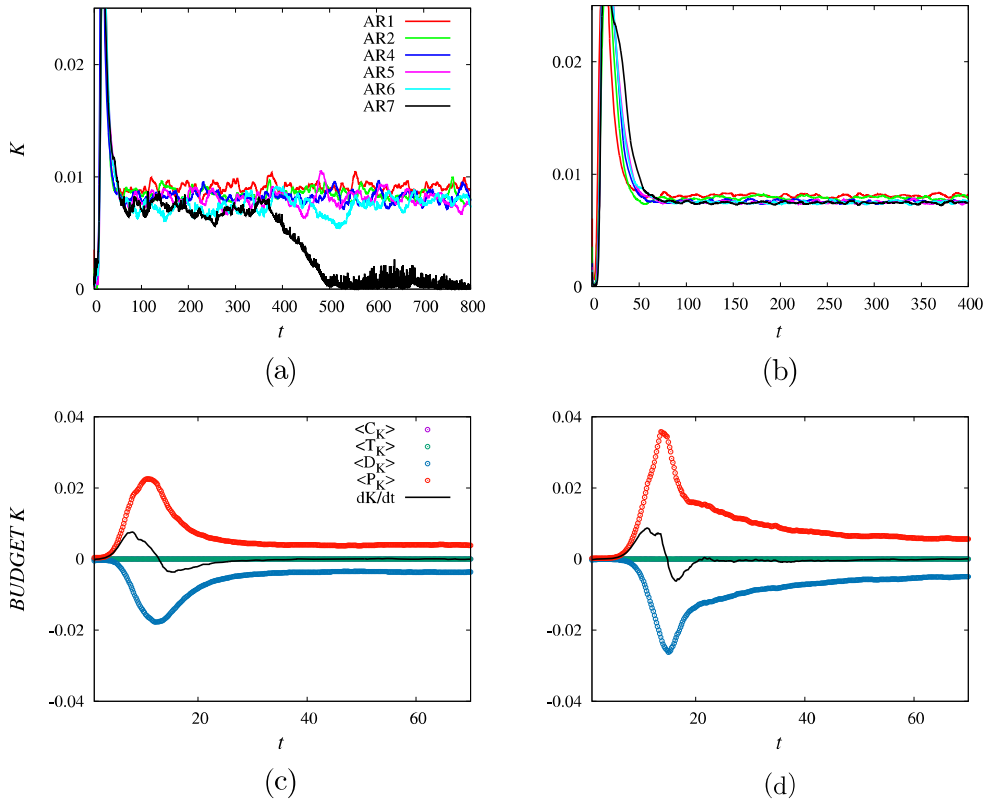

Figure 3. Time evolution of turbulence kinetic energy at $Re = 2500$ (a) and $Re = 7750$ (b), and budget of K at $Re = 5000$ for $A_R = 1$ (c) and $A_R = 7$ (d). Each budget term is indicated in the legend of panel (c).

increase or decrease of the streamwise velocity gradients near the walls, resulting in the behaviour of Π shown in Figure 2. Hence, it may be expected that a similar time evolution is also encountered for the total turbulence kinetic energy $K = \langle q \rangle = \langle \overline{u_i u_i}/2 \rangle$, where carets now denote averaging over the duct cross-section, $\langle A \rangle = (1/L_2 L_3) \int\int A \, \mathrm{d}x_2 \, \mathrm{d}x_3$. A similar behaviour is observed at low and high Reynolds number, as shown in Figure 3(a,b), and similarity with the pressure gradient in Figure 2 is also evident. Both quantities in fact attain a maximum at early times, and after a decrease enter a final stage characterised by oscillations around their steady-state value. The complex flow physics in the initial stages of flow development can be investigated by looking at the evolution of the various terms in Equation (2). The integrated budgets are shown in Figure 3(c,d), in which only P_K and D_K yield non-zero contribution. These figures have been evaluated at $Re = 5000$, intermediate between those considered in Figures 2, 3(a) and 3(b). In the first 15 time units $\langle P_K \rangle$ exceeds $\langle D_K \rangle$, hence K grows exponentially up to $t \approx 10$. Later on $\langle P_K \rangle$ and $\langle D_K \rangle$ reach a maximum, which is soon followed by the maximum of K. For $A_R = 7$ the behaviour is similar, but in this case the values of $\langle P_K \rangle$ and $\langle D_K \rangle$ are larger, promoting more rapid increase and decrease of K. This is reasonable, since the shorter side of the duct is driving the process, hence energy grows in a large number of small-sized structures in the duct cross section. The final result, for any aspect ratio, is that after the transient $\langle P_K \rangle$ and $\langle D_K \rangle$ equilibrate, and $\mathrm{d}K/\mathrm{d}t$ becomes small.

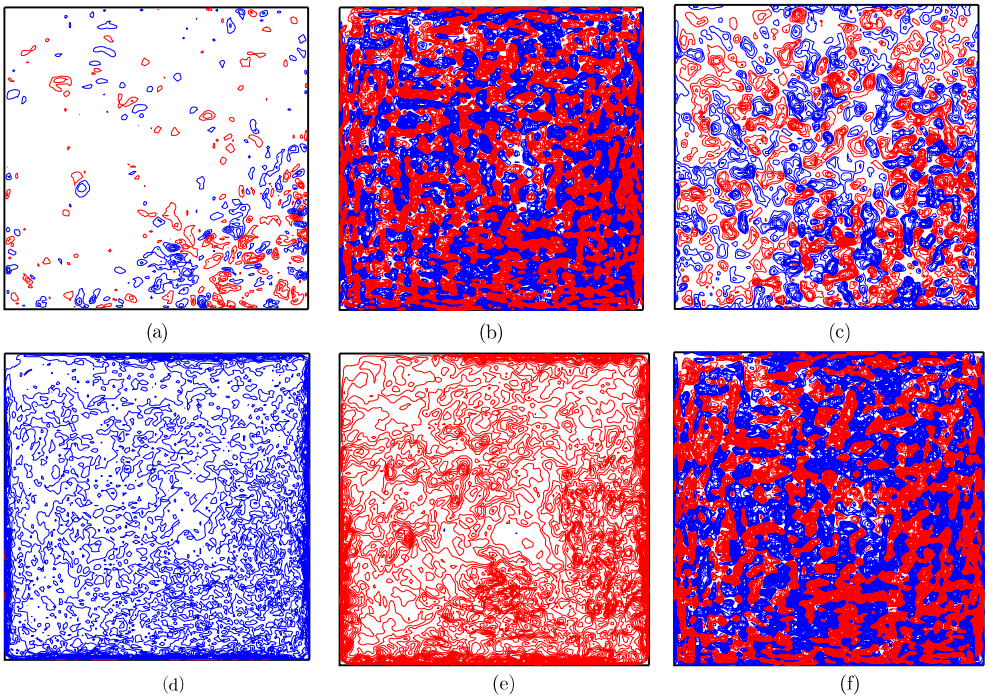

Figure 4. Contours of budget terms in equation (2) at $t = 15$, for $A_R = 1$, $Re = 5000$. (a) C_K, (b) T_{KT} (c) T_{KP}, (d) D_K, (e) P_K, (f) dq/dt; red positive, blue negative, spaced by $\Delta = 0.02$.

Deeper insight into the flow dynamics is provided by the maps of the budget terms in the duct cross section, shown in Figure 4 at $t = 15$, and in Figure 5 at $t = 60$, for the case $A_R = 1$, $Re = 5000$, which allows clearer visualisation of the flow structures. These figures clearly show that, although their integrated contribution is zero, large values of the convective (C_K) and of the turbulent diffusion ($T_K = T_{KT} + T_{KP}$) terms occur. Among these contributions, the one associated with the triple velocity correlations T_{KT} is largest. Whereas at steady state the flow structures are located near the walls, a much more uniform distribution is observed at $t \approx 15$. Figure 4 shows that, with the exception of C_K, all the other terms are distributed over the entire cross section of the duct. The regions with high production (Figure 4(e)) coincide quite well with regions of high dissipation (Figure 4(d)), as can be more clearly observed in the region close to the right top angle.

The correlation coefficient between $T_q = dq/dt$ and each budget term of equation (2) allows to quantify the different contributions. We have then evaluated $TC_K = C_K + T_K$, $PD_K = P_K + D_K$, T_q, at each point over the duct cross. Their fluctuations with respect to the averaged values, namely $TC'_K = TC_K - \langle TC_K >$, $PD'_K = PD_K - \langle PD_K >$, $T'_q = T_q - \langle T_q \rangle$, allow to evaluate the correlation coefficients

$$C_{TT} = \frac{\langle T'_q TC'_K \rangle}{\sqrt{\langle T'^2_q \rangle \langle TC'^2_K \rangle}}, \quad C_{TP} = \frac{\langle T'_q PD'_K \rangle}{\sqrt{\langle T'^2_q \rangle \langle PD'^2_K \rangle}}.$$

At $t = 15$, we find $C_{TT} = 0.96$, $C_{TP} = 0.39$, which implies that the point-wise variations of q are mainly due to transfer of turbulence from one region of the duct to another.

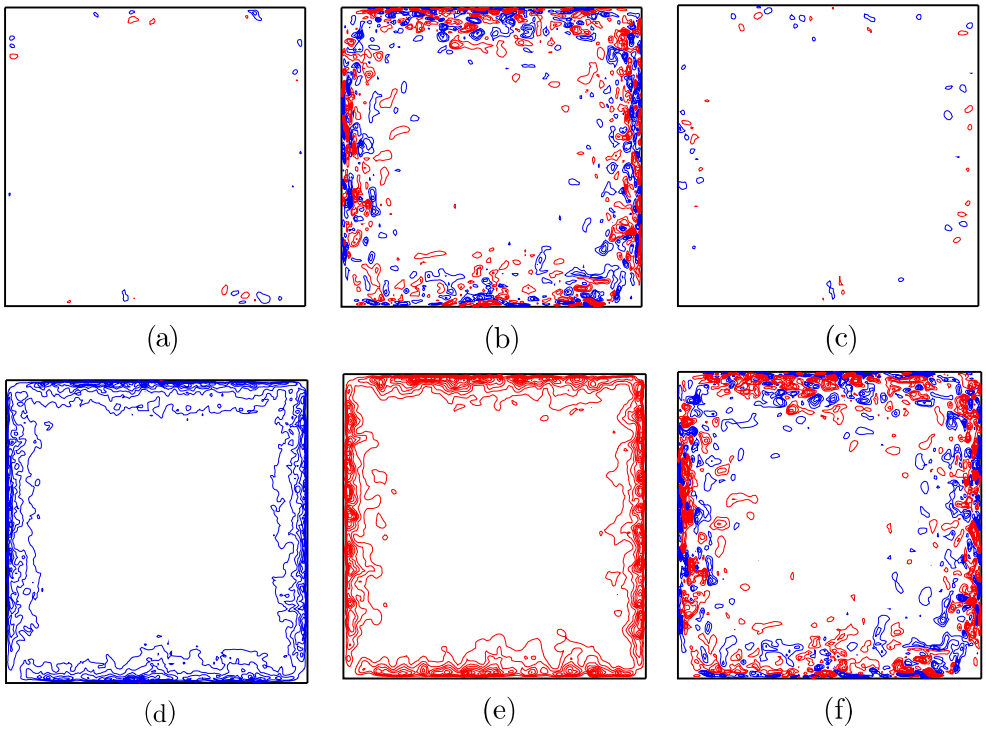

Figure 5. Contours of budget terms in equation (2) at $t = 60$, for $A_R = 1$, $Re = 5000$. (a) C_K, (b) T_{KT} (c) T_{KP}, (d) D_K, (e) P_K, (f) dq/dt; red positive, blue negative, spaced by $\Delta = 0.02$.

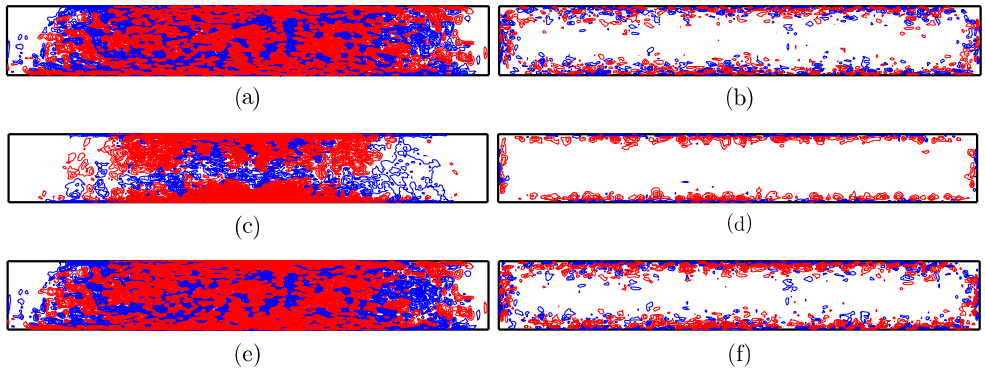

Figure 6. Contours of budget terms in equation (2) at $t = 15$ (left) and at $t = 60$ (right), for $A_R = 7$, $Re = 5000$. (a) and (b) TC_K, (c) and (d) PD_K, (e) and (f) T_q; red positive, blue negative, spaced by $\Delta = 0.02$.

Figure 5, at the end of the initial transient, shows a completely different scenario. In fact, as expected in any kind of wall-bounded flows, the flow dynamics is concentrated near walls. Figure 5 shows that C_K and T_{KP} reduce in amplitude, whereas the contribution of the triple correlations T_{KT} is still large, being quite similar to the distribution of T_q. P_K and D_K are mainly concentrated near the walls, which implies local equilibration between production and rate of turbulence kinetic energy dissipation. At this time, the values of the

correlation coefficients are $C_{TT} = 0.86$, $C_{TP} = 0.54$, implying again that local time variation of kinetic energy is linked to transfer, rather than to the net effect of production and dissipation. Minor differences are found in the case of rectangular ducts, for which the values of the correlation coefficients are $C_{TT} = 0.91$, $C_{TP} = 0.45$ at $t = 15$, and $C_{TT} = 0.79$, $C_{TP} = 0.62$ at $t = 60$.

Similarities and differences between square and rectangular ducts may be traced by looking at Figure 6, in which we show the distributions of TC_K, PD_K and T_q for a rectangular duct with $AR = 7$. Clear association between transport term and time variation of q is also observed in this case, both at early and at late times. Turbulence in this case is seen to form initially in the duct core and away from the short sides, and to migrate towards all four walls at later times. Interestingly, at early times we find excess of production over dissipation near the walls, and the opposite in the duct centre, whereas the opposite is found at later times.

3.2. Friction factor

We previously mentioned that in rectangular channels the Reynolds number based on the short side half length marks the transition from the laminar to the turbulent regime. To demonstrate that C_f has a nearly universal behaviour with Re_3 both in the laminar and in the turbulent regime, in Figure 7 we show the maps of C_f versus the three Reynolds number indicated in Table 1. The common feature is a satisfactory collapse of the data in the fully turbulent regime, regardless of the definition of the Reynolds number. The present results show the same trend as those in laboratory experiments at higher Reynolds number [24] and also agree with previous numerical simulations at intermediate Re_3 for $A_R = 1 - 7$ [1]. On the other hand, in the laminar regime the poorest scaling is obtained with Re (Figure 7 a), which may be understood because the choice of a reference length based on the radius of an equivalent pipe does not account for the shape of the duct. In the three figures, lines with the same colour as the solid symbols are evaluated from the analytical expression (3-48) given at p.113 of White [14]. Also the classical Reynolds number based on the hydraulic diameter is not suitable to account for the shape of the duct cross section, as may be inferred from Figure 7(b). On the other hand, the choice of the short side as the reference length yields good collapse both in the laminar and in the turbulent regime. Regardless of the aspect ratio, the transitional Reynolds number is found at $Re_3 \approx 850$, as may be seen in the inset of Figure 7(c). This value is not very different from that reported by Takeishi et al. [13], who found transition to occur at $Re_3 \approx 700$, regardless of the duct aspect ratio. The difference may be due to the different initial conditions and to the shorter streamwise duct length. In this figure, it may be noticed that the behaviour for $A_R = 1$ (the red solid symbols) is a bit different, which probably implies that the absence of symmetry about the corner bisector in rectangular ducts generates stronger disturbances due to the secondary motion, which cause earlier transition.

3.3. Wall friction and secondary motions

In the subsequent part of the paper, all statistical quantities are evaluated by performing averages in the streamwise directions and in time, with the number of realisations N_f given in Table 1. Local wall units are indicated with the $+$ superscript.

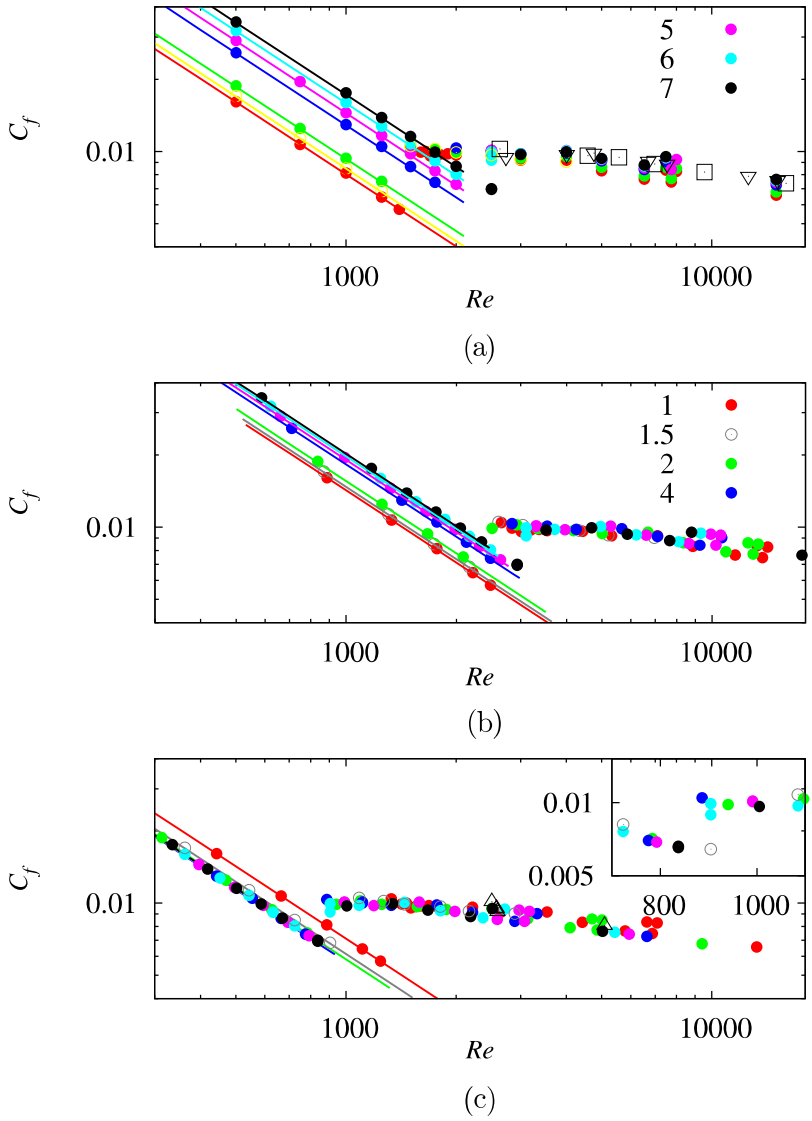

Figure 7. Rectangular ducts: friction coefficient C_f versus (a) computational Reynolds number Re; (b) Reynolds number based on the hydraulic diameter Re_D; (c) Reynolds number based on the short side half-length. The aspect ratio A_R is indicated in the legend of panels (a) and (b), and a zoom around the transitional Re is shown in panel (c); the solid lines correspond to equation (3-48) of White [14]; in (a) the open symbols are taken from Hartnett et al. [24], triangles $A_R = 10$, squares $A_R = 5$; in (c) open triangles are taken from Vinuesa et al. [1].

To understand the previously discussed behaviour of the mean friction coefficient, it is worth analysing the distributions of the secondary stream function and the local wall shear stress in the passage from laminar through the transitional to the fully turbulent regimes. In particular, in Figure 8 we show the profiles of the wall shear stress, $\tau_w = S_n/Re$, and of the wall-normal velocity gradient, $S_n = \mathrm{d}U_1/\mathrm{d}n|_w$, as a function of the distance from the corner (s). Data are shown here for the representative case of a square duct, all other cases being

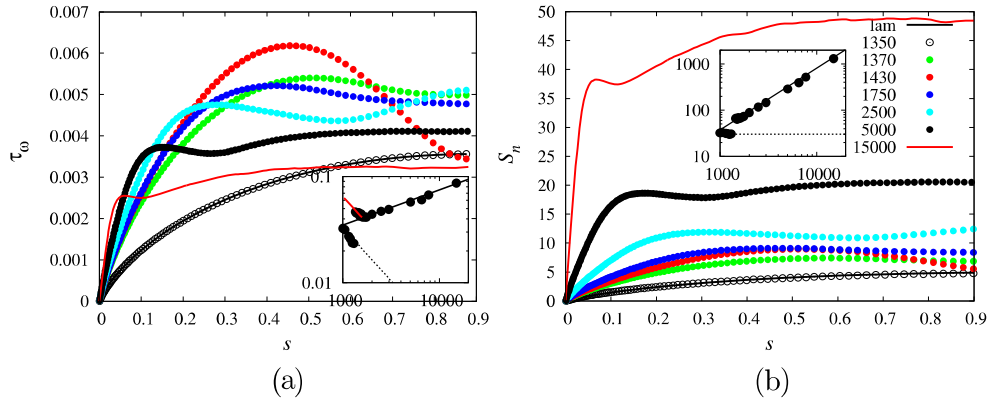

Figure 8. Square duct ($A_R = 1$): profiles of (a) wall shear stress, τ_w and (b) wall-normal velocity gradient, S_n, at the wall, versus the distance from the corner (s), at different Re, as listed in the legend of panel (b); in the inset of (a) we show the gradient of τ_w at $s = 0$, and in the inset of (b) we show S_n at $s = 0$.

quite similar. Figure 8(a) shows that τ_w is zero at the corner ($s = 0$), and the secondary motions dictate different trends near the corners. As expected, the velocity gradients in the laminar regime do not depend on the Reynolds numbers. In particular, Figure 8(b) shows that at $Re = 1300$, S_n is in perfect agreement with the analytical expression given at p. 113 of White [14]. On the other hand, in the transitional and turbulent regime, S_n grows with different trends depending on the Reynolds number. The slope near the corner is plotted in the inset of Figure 8(b), which shows a growth proportional to $Re^{4/3}$. Accordingly, the gradient of τ_w grows as $Re^{1/3}$ in the fully turbulent regime, as shown in the inset of Figure 8(a). In the transitional regime, the variation of $\mathrm{d}\tau_w/\mathrm{d}r|_{s=0}$ with Re equals that in the laminar regime, as given by the red line in the inset of Figure 8(a). The transitional regime ends at $Re = 1600$, and from $Re = 1750$ the values of $\mathrm{d}\tau_w/\mathrm{d}r|_{s=0}$ are aligned with those at higher Re. Strong shape variation in the various flow regimes are apparent. In the laminar regime, τ_w decreases linearly, as predicted by equation (3-47) of White [14, p.113]. In the transitional regime, a maximum of τ_w occurs at distance $s = 0.5$ from the corner (red dots in in Figure 8 a). Increasing Re two peaks appear, which are well depicted by the blue and black dots in Figure 8(a). One of the peaks moves closer to the corner at higher Re, whereas the other nearly remains at the centre of the duct side, with small oscillations in a region which becomes wider at higher Re. At sufficiently high Re, the wall friction profiles shown in Figure 8(a), are equivalent to those at higher Re, as reported by Pirozzoli et al. [16].

To better understand the differences noted above, and see whether the statistical quantities reproduce the expected symmetries it is worth looking at the contours of the stream-function of the mean secondary motion superimposed to the mean vorticity components ($\langle\Omega_2\rangle = \partial U_1/\partial x_3$, $\langle-\Omega_3\rangle = \partial U_1/\partial x_2$), divided by the Reynolds number, over the entire duct cross section. It is important to keep in mind that the $\langle\Omega_i\rangle$ contribute to turbulence kinetic energy production, to be discussed later on. When averaged on all the duct walls, viscous strain returns the wall shear stress distributions shown in Figure 8(a). The profiles of τ_w along the whole duct perimeter are shown in Figure 9, under the corresponding stream function and vorticity contours. In the laminar regime (Figure 9 a), characterised

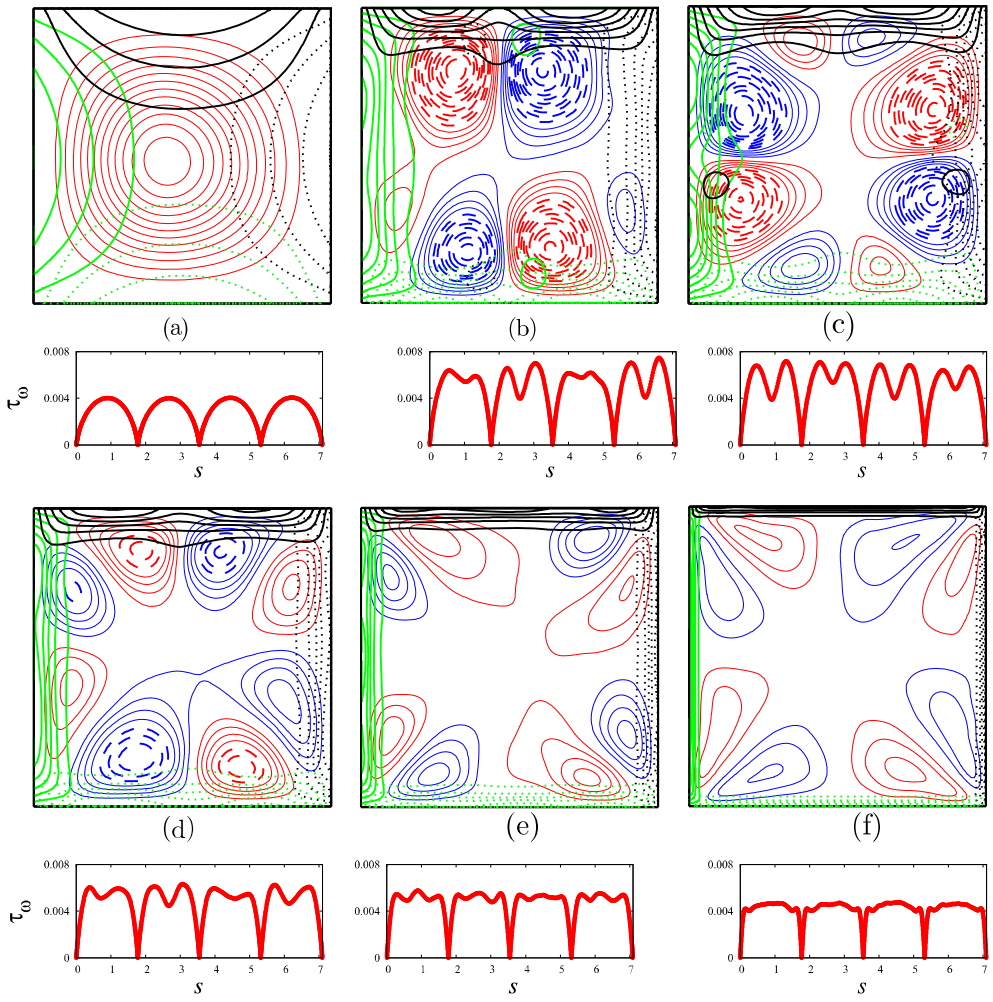

Figure 9. Iso-lines of Ω_2/Re and Ω_3/Re (with spacing $\Delta = 0.001$ green positive dotted, black negative solid), superimposed to iso-lines of the secondary stream-function ψ (with spacing $\Delta = 0.0005$ thin up to .002 from 0.025 thick lines red positive blue negative), at different *Re*. In panel (a), $\Delta\psi = 10^{-6}$. The small figures under each panel show τ_W along the perimeter of the duct. The Reynolds numbers are (a) 1350, (b) 1370, (c) 1430, (d) 1750, (e) 2500, (f) 5000.

by the absence of secondary motions, the U_1 contours do not change with *Re*. The mean strain decreases moving from the walls towards the central region. Immediately after the critical Reynolds number, $Re_C \approx 1350$, the secondary motion consists of four recirculating regions, that, at high *Re*, yields the well documented pattern with eight eddies. In Figure 9, the increments of the stream-function contours have been maintained fix for all the Reynolds numbers, hence the comparison among the different regimes leads to the conclusion that the strength of the secondary motion decreases in the transitional and in the fully turbulent regimes by increasing *Re*, up to $Re = 5000$. At higher *Re*, the strength does not change very much. To emphasise that the flow structures change in a sharp range of Reynolds number near Re_C, visualisations are shown at $Re = 1370$ in Figure 9(b), and

at $Re = 1430$ in Figure 9(c). These figures demonstrate that there is an equal probability to have secondary structures in one or in the other side, depending on the growth of disturbances either near one or the other side, during the initial transient. Animations allow to see the different time history, and where disturbances form and grow. A slight increase of Reynolds number ($Re = 1430$) yields a secondary motion with four pairs of large-scale structures, two strong and two weak (Figure 9(c)). It has been observed by the time history of the mean pressure gradient Π and of the total turbulence kinetic energy $K = \langle u_i' u_i' \rangle / 2$, that the convergence to a steady state requires simulations lasting for very long time. At $Re = 1750$, Figure 9(d) shows that the intensity of the four couples tends to be the same, and that the magnitude of τ_w along the perimeter is slightly reduced with respect to that at $Re = 1430$. At this Re, the inset of Figure 2(a) shows the start of the tendency towards the Blasius law corresponding to a fully turbulent regime, which is characterised by a secondary motion with four pairs of recirculating regions. The size of the secondary structures is comparable to half of the wall length, hence they can transport U_1 towards the wall at $r = L_2/4$ and far from the wall at $r = L_2/2$. Further increase of the Reynolds number ($Re = 2500$) yields (Figure 9(e)) reduction of the strength of the secondary structures, which in addition become confined to the duct corners. Two maxima appear in the profiles of τ_w, and their amplitude decreases as was observed in Figure 8(a). The thickness of the vorticity layers in Figure 9(f), at $Re = 5000$, reduces, implying that the near-wall turbulence is not largely affected by secondary motion. This behaviour continues by increasing the Reynolds number.

The influence of the duct aspect ratio on the structure of the secondary flow and on the wall shear stress in the fully turbulent regime ($Re = 5000$) is analysed in Figure 10. In that figure both directions are normalised by $L_3/2$, hence the vertical coordinate ranges from -1 to $+1$. Comparison between Figure 10(a) (for $A_R = 1$) and Figure 10(b) (for $A_R = 2$) shows that the recirculating region near the short vertical wall reduces in size and strength. On the other hand, the recirculating region near the horizontal wall increases in size and strength. This asymmetry causes the formation of strong disturbances propagating from the corner towards the central region, which explains why the critical Reynolds number in square ducts is higher than in rectangular ducts. The growth of the stronger recirculation and the location of the maximum is fixed, which suggests that L_3 is the appropriate length scale at low Reynolds numbers. However, transition to the turbulent regime does not occur without the small recirculating region near the short side. This was observed in similar plots at $Re = 2500$ (not shown) and is corroborated by the C_f plots of Figure 7, where the black dots corresponding to $A_R = 7$ at $Re = 2500$ are aligned with the laminar values. Although barely visible in the profiles of $\tau_w(s)$ for $A_R = 7$, at $Re \leq 2500$ there is only one peak along the short side, whereas at $Re = 5000$ there are two peaks which are associated with the secondary recirculating regions near the short side. At $Re = 2500$, $A_R = 6$, two peaks with small undulations arise, which are sufficient to have C_f in Figure 7 no longer aligned with the laminar trend. At $A_R = 5$, the two peaks are visible in Figure 10 of $\tau_w(s)$ at $Re = 2500$, hence the corresponding value of C_f in Figure 7 coincides with the values of the simulations with smaller aspect ratio. At $A_R = 5$ the profiles of $\tau_w(s)$ only have one peak in the short side at $Re = 1750$, which is found also for $A_R = 4$, and two peaks finally form for $A_R = 2$ as confirmed in Figure 7(a), where at $Re = 1750$ the value of C_f is not aligned with the laminar trend.

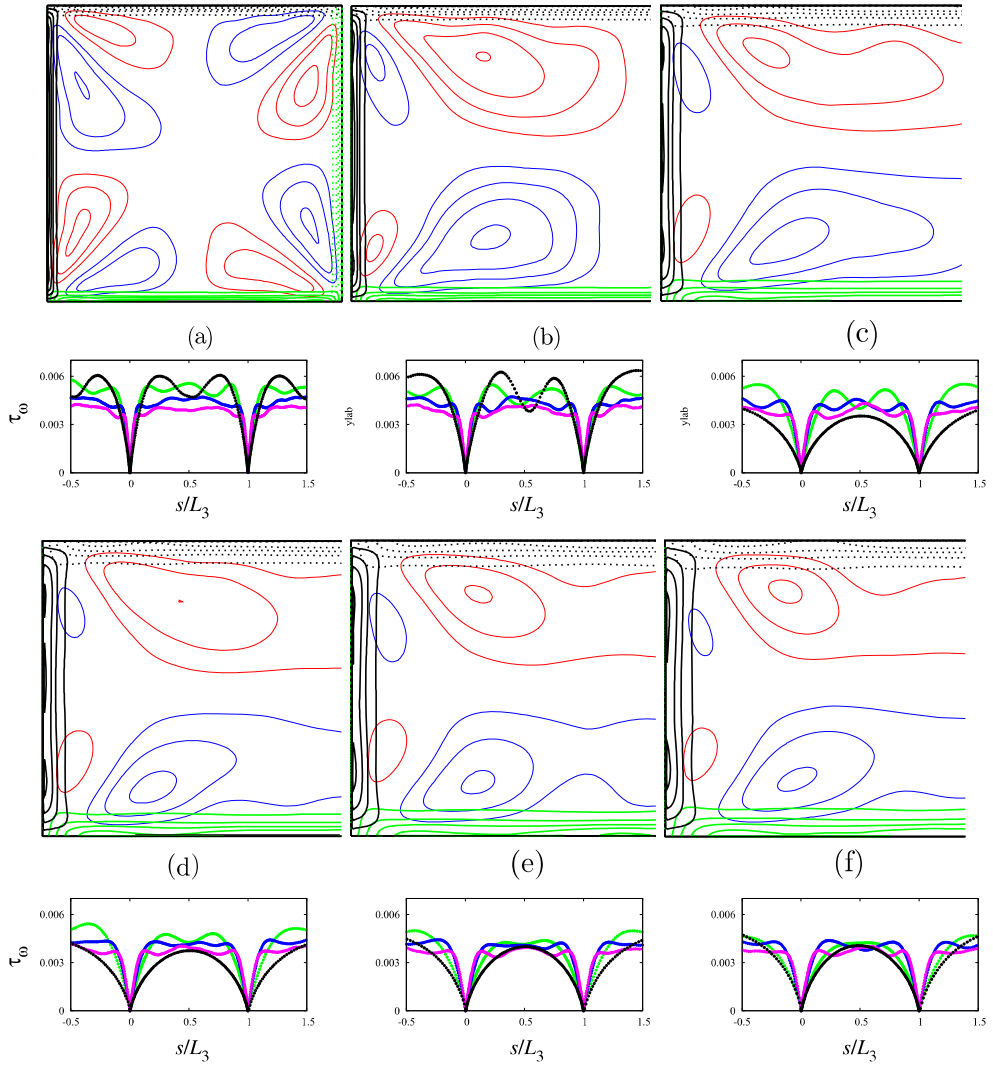

Figure 10. Rectangular ducts: contours of vorticity components ω_2 and ω_3, superimposed to the secondary stream-function ψ at $Re = 5000$ and various aspect ratios, (a) $A_R = 1$, (b) $A_R = 2$, (c) $A_R = 4$, (d) $A_R = 5$, (e) $A_R = 6$, (f) $A_R = 7$. The small panels under each figure show the wall shear stress (τ_w) along part of the duct perimeter, to show more clearly the behaviour along the short side. The data are shown at $Re = 1750$ (black), at $Re = 2500$ (green), $Re = 5000$ (blue), $Re = 7750$ (cyan).

3.4. Mean flow

The flow near the corner in rectangular ducts does not change dramatically from the case of square ducts. Contours of U_1^+, q^+ ω_1^+ and ψ^+ in the corner regions are shown in Figure 11, at fixed $Re = 5000$, for different values of the aspect ratio, superimposed to each other to have a global picture of whether the behaviour is drastically affected. The two space coordinates and all quantities are here scaled with the averaged friction velocity. The contours of U_1^+ (Figure 11a) are superimposed each other, especially near walls, whereas some difference may be appreciated far from the walls near the shorter side. Increasing the aspect ratio

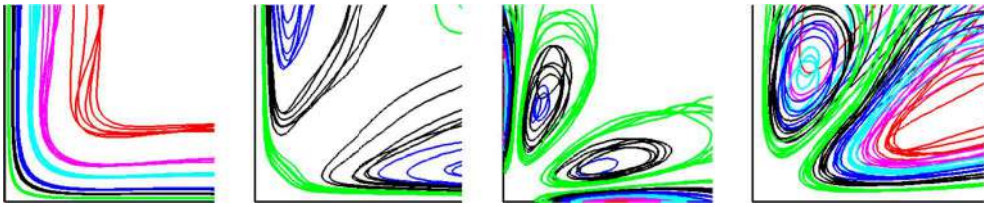

a) b) c) d)

Figure 11. Rectangular duct: contours of (a) U_1^+, green 2 black 4 blue 6 cyan 10 mag 12 red 14; (b) q^+ green 1 black 2 blue 3; (c) ω_1^+ green .01 black .02 blue .03 cyan .04 mag .05 red .06; (b) ψ^+ green 1 black 2 blue 3 cyan 4 mag 5. All data are shown at $Re = 5000$ for $A_R = 1$, $A_R = 2$, $A_R = 4$, $A_R = 5$, $A_R = 6$, $A_R = 7$. Space coordinates are scaled with respect to the averaged friction velocity, $\overline{u_\tau}$.

to $A_R = 4$ the $U_1^+ = 14$ iso-line (red) moves parallel towards the central region. Further increasing A_R, the $U_1^+ = 14$ iso-line near the bisector moves towards the short side of the duct. In the long side region, the contours are flat near the wall, and undulations appear far from the wall. The turbulence kinetic energy distributions near the walls are independent of the aspect ratio, as shown by the green lines ($q^+ = 1$) in Figure 11(b). On the other hand, the blue contours ($q^+ = 3$), in the long side region move far from the corner by increasing A_R. In this region, also the black contours ($q^+ = 2$) shrink indicating large variations of the turbulence kinetic energy distribution. In the short side region, small variations are seen in Figure 11(b). This behaviour might be ascribed to the effect of the secondary motion, but in fact the contours of ω_1^+ in Figure 11(c) show only marginal variation with A_R. This vorticity component is linked to the small scales in the near-wall region. The strong vorticity layers attached to the horizontal and vertical walls are found to scale well with the averaged friction velocity. The large-scale secondary motion depicted through the stream function in Figure 11(d), consists on two recirculating regions of different size, the bigger one along the long side. It is important to stress that asymmetry appears only for $A_R > 1$, and in agreement with the previous discussion, disappears at $A_R = 1$.

At statistically steady state, it is interesting to analyse the profiles of the mean streamwise velocity U_1 in wall units to see whether they behave as those in the two-dimensional turbulent plane channel. For square ducts [16] reported similar profiles scaled both with the mean u_τ and with the local u_τ with the result to have in the latter case a better scaling. Here we would like to see whether the local scaling gives good scaling both for the profiles along the long and short walls. For the square duct, the profiles are evaluated starting from the wall ending to the bisector. For the symmetry, no differences should be expected between the two walls. In the rectangular channel, the profiles along the short side end on the bisector, on the other hand along the long wall, for a distance equal to that of the short wall end on the bisector, later on end on the middle line. Therefore along the long wall a greater number of profiles is plotted, in accordance with the values of the blue symbols given in the legend of Figure 12. Orlandi et al. [7] reported the profiles in wall units for the canonical channel up to $R_\tau = 4000$ showing that is parabolic up to $R_\tau \approx 77$, and at slightly greater R_τ ($R_\tau = 180$) attains larger values than those at higher Re_τ, for the same value of y^+.At this Reynolds number, there is no separation between outer and near-wall structures, and a single very large unsteady eddy is present, causing the overshoot with respect the canonical

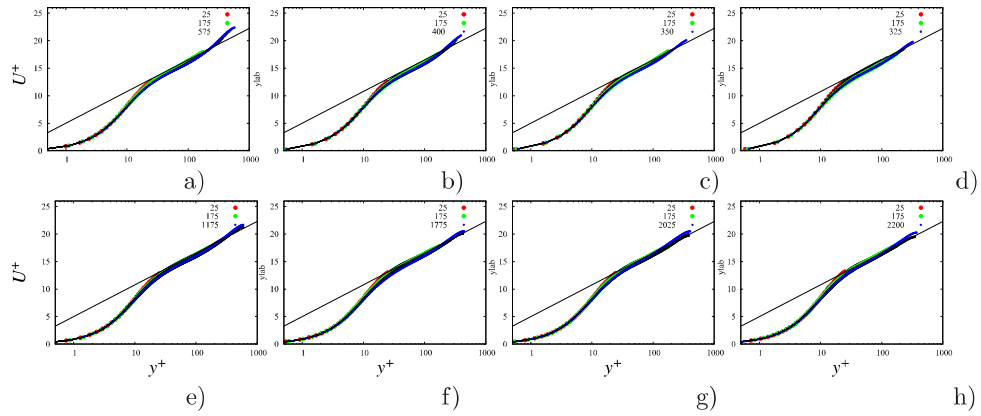

Figure 12. Profiles of the mean velocity in wall units (here the τ varies along the walls accordingly to the profiles of τ_w in Figure 10) at $Re = 15,000$; top figures profiles along the long the wall, bottom along the short wall, each black line is for profiles separated by $d^+ = 25$ wall units, the solid symbols are for profiles at the distance d^+ given in the legend, the duct with the following aspect ratio were considered: (a,e) $A_R = 2$, (b,f) $A_R = 4$, (c,g) $A_R = 5$, (d,h) $A_R = 6$.

logarithmic velocity profile. From the data at $Re = 2500$, not reported, the same overshoot occurs in ducts at all locations, hence also at a position corresponding to $Re_\tau = 25$, which would be too low to have fully turbulent flow in a two-dimensional channel. The formation of a mean velocity profile similar to that of fully turbulent flows is therefore due to the dynamics of the near-wall structures produced in the neighbouring regions. This explains why the U_1^+ profile at $Re_\tau = 25$ obtained from the simulation at $Re = 15,000$ does not show the overshoot in Figure 12. Some difference may be observed in the wake region, mainly due to evaluation of the profiles up to the diagonal line in the rectangular duct in particular at high A_R. The global result is that indeed for rectangular ducts, at high Re, a good scaling with the local u_τ is found and that flows in rectangular ducts allow to investigate the Reynolds number dependency through a reduced number of simulations. The validity of local wall scaling was originally discussed by Gavrilakis [15] at low Re, and by Pirozzoli et al. [16] at much higher Re, for the case of square duct. Here we confirm that it also holds for rectangular ducts. At low Re, the mean velocity profiles differ from those in the two-dimensional channel due to the interaction of flow structures of different size.

3.5. Turbulence kinetic energy budgets

The good scaling in wall units of the mean motion U_1^+, of the secondary motion through ω_1^+, and of the turbulence kinetic energy q^+, and their rather good independence on the aspect ratio, is also found for each term of the simplified turbulence kinetic energy budget, shown in Figure 13. This budget is given by an equation similar to that in Equation (2)

$$0 = \widehat{C_K} + \widehat{T_K} + \widehat{D_K} + \widehat{P_K} \tag{3}$$

the hat, omitted in the rest of the paper, indicates averages in x_1, among the four quadrants and in time with realisations taken after the transient, described in Section 3.1. In this way, the left-hand side is null. The DNS results depict the occurrence of large values for D_K^+

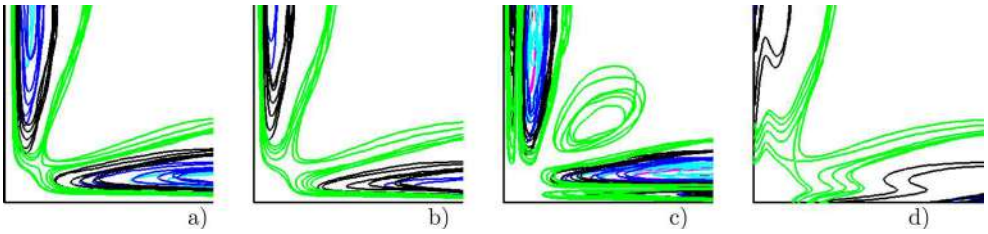

Figure 13. Rectangular duct: contours of (a) P_K^+; (b) D_K^+; (c) $T_K^+ + C_k^+$, green $\pm = .0125$, black $\pm = .025$, blue $\pm = .0375$, cyan $\pm = .05$, magenta $\pm = .0625$, red $\pm = .075$, solid positive and dotted negative; (d) ϵ_K^+. In panels (a), (b) and (d) green $\pm = .05$, black $\pm = .1$, blue $\pm = .15$, cyan $\pm = .2$, magenta $\pm = .25$, red $\pm = .3$, solid positive dotted negative. All data are shown at $Re = 5000$ for $A_R = 1$, $A_R = 2$, $A_R = 4$, $A_R = 5$, $A_R = 6$, $A_R = 7$. Space coordinates are scaled with respect to the averaged friction velocity, $\overline{u_\tau}$.

and P_K^+ near the walls, with those of D_K^+ closer to the walls than those of P_K^+. The latter has its peak far from the corner at a distance from the walls approximately 15 wall units. The good equilibrium between production and total dissipation is corroborated by the small values of $T_K^+ + C_K^+$. Figure 13(c) further shows alternation of negative and positive layers near the walls, depending on the relative magnitude of P_K^+ and D_K^+. The rather good scaling of the isotropic dissipation rate ϵ_K^+ in wall units arises in Figure 13(d). Comparison between this figure and Figure 13(b) demonstrates that modelling D_K^+ should be easier than modelling ϵ_K^+.

To investigate whether the scaling in wall units holds by increasing the Reynolds number, in Figure 14 we show the contours, of mean velocity, turbulence kinetic energy and terms of the turbulence kinetic energy budget, for $A_R = 1$. Comparison of the U_1^+ contours demonstrates that the distortion is greater at lower Re, implying that the influence of the secondary motion is stronger, in large part of the quadrant. At high Reynolds numbers ($Re = 7750$ and 15,000) the contours are quite similar, and similar variations of q^+ may be observed at all Re. The panels reporting P_K^+ and D_k^+ show once more good balance between turbulence kinetic energy production and total dissipation. The regions with D_K^+ higher than P_K^+ correspond to the thin regions with negative C_K^+ near the two walls. Far from the corner and in the region close to the corner bisector D_K^+ slightly overcomes P_k^+, however, this is a region with weak turbulence according to the contours of q^+. The results shown in Figure 14 emphasise a good scaling in wall units of mean motion, turbulence and budgets in a square duct. Linear scales used here allow to analyse the behaviour far from the corner.

It is thus worth analysing whether mean and turbulent quantities also scale with the mean friction velocity for $A_R \neq 1$. A rectangular duct with $A_R = 7$ has been considered to compare the distribution of the various quantities with those in Figure 14, at $Re = 7750$ and $Re = 15,000$. However, for $A_R = 7$, $Re = 2500$, the flow is laminar, as may be argued from the C_f shown in Figure 7(a) (black dots). On the other hand, turbulent flow is found at $A_R = 6$, $Re = 2500$, thus in Figure 15 we show the behaviour of the quantities at $Re = 2500$ for $A_R = 6$. At this low Re, the choice to analyse a $100^+ \times 100^+$ box around the corner leads to a vertical size in the top panels of Figure 15 which is shorter than the horizontal one, in fact $L_3^+/2 = 61$, whereas $L_2^+/2 = 367$. These differences, in particular in the turbulence kinetic energy, lead to different distributions close to the horizontal and vertical walls. The

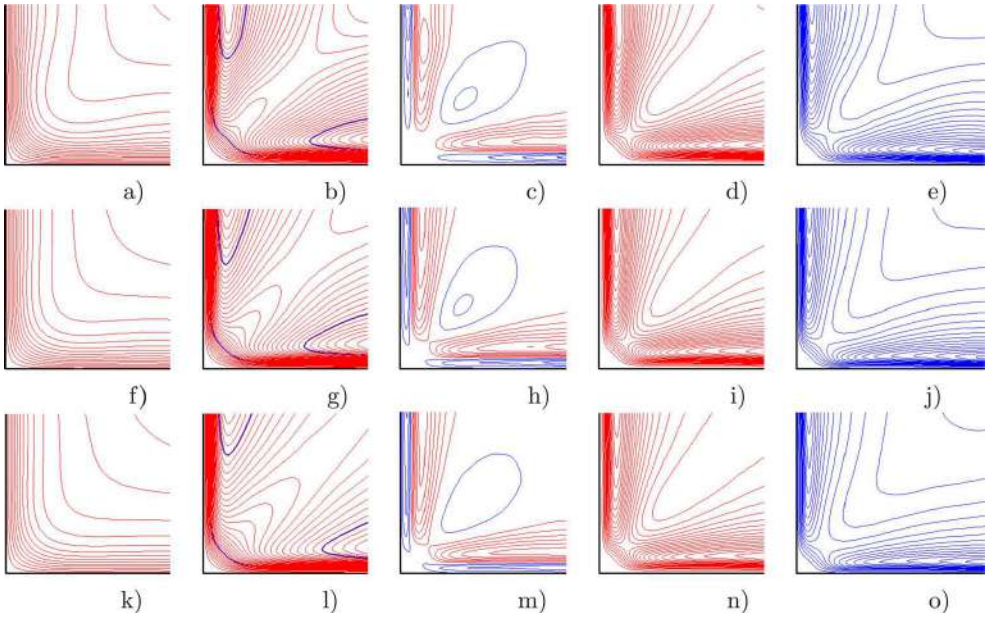

Figure 14. Rectangular duct ($A_R = 1$): contours of U_1^+ (a,f,k); q^+ (b,g,l), $C_K^+ + T_K^+$ (c,h,m), P_K^+ (d,i,n), D_K^+ (e,j,o), at $Re = 2500$ (a–e), $Re = 7750$ (f–j), $Re = 15000$ (k–o). Only a $100^+ \times 100^+$ box is shown near the corner. Positive contours are shown in red, and negative in blue, with increments $\Delta = 1$ for U_1^+ and q^+, and $\Delta = .001$ for the budgets terms. The blue line denotes $q^+ = 1$.

blue line in Figure 15(b), corresponding to $q^+ = 1$, near the vertical wall is localised in a smaller region than that near the horizontal wall. This is corroborated by the contours of P_K^+ in Figure 15(d) and of D_K^+ in Figure 15(e). The total dissipation D_K^+ near the vertical wall does not overcome P_k^+, whereas this occur near the horizontal wall, and this difference may be also inferred from the contours of $C_K^+ + T_K^+$ in Figure 15(c). At $Re = 7750$, $L_3^+/2 = 170$, hence the $100^+ \times 100^+$ box should not show large differences near the walls. Indeed, both the contours of U_1^+ and q^+ in the middle panels show better symmetry around the corner bisector. Symmetry is further supported by the distributions of the three terms in the turbulence kinetic energy budget, which are very similar to those at the same Re in Figure 14. Visualisations in a wider region show that at larger wall distances than 100^+, all quantities do not change and behave similarly near walls. This explains why C_f in the fully turbulent regime scales well regardless of the definition of Reynolds number. At $Re = 15,000$, $L_3^+/2 = 310$, hence in bottom figures the contours close to the corners show better symmetry than that at $Re = 7750$. From Figure 15, it may be asserted that at high Reynolds number, that is in the fully turbulent regime, mean and turbulent motion scale well with the averaged friction velocity also for rectangular ducts. Under these conditions, the corrections caused by the corner are concentrated in a small region, and large part of the duct is occupied by turbulent flow not different from a canonical planar channel. Completely different is the behaviour near the transitional Reynolds number, in which the corner bisector symmetry is lost. In ducts with high aspect ratios, the near-wall structures are constrained near the short side, thus turbulence is not sustained, and although the other side is long enough, q^+ remains nearly zero.

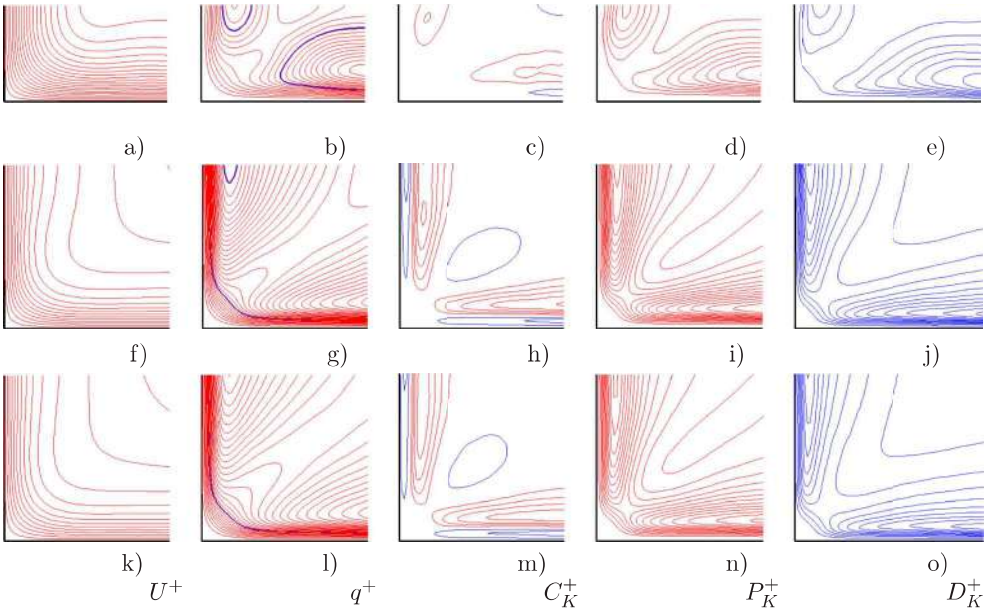

Figure 15. Rectangular duct: contours of U_1^+ (a,f,k); q^+ (b,g,l), $C_K^+ + T_K^+$ (c,h,m), P_K^+ (d,i,n), D_K^+ (e,j,o), at $Re = 2500$, $A_R = 6$ (a–e), $Re = 7750$, $A_R = 7$ (f–j), $Re = 15000$, $A_R = 7$ (k–o). Only a $100^+ \times 100^+$ box is shown near the corner. Positive contours are shown in red, and negative in blue, with increments $\Delta = 1$ for U_1^+ and q^+, and $\Delta = .001$ for the budgets terms. The blue line denotes $q^+ = 1$.

3.6. Turbulent stresses in principal mean strain axes

The profiles of the *rms* velocity fluctuations in channels and ducts show large anisotropy, which may be ascribed to differences in the respective production, resulting from interaction of the mean strain-rate tensor $S_{ij} = (\partial U_i/\partial x_j + \partial U_j/\partial x_i)/2$, and the Reynolds stress tensor $R_{ij} = -\langle u_i u_j \rangle$. In particular, the production term in the turbulent stresses transport equation is $P_{ij} = -(R_{ik}(\partial U_j/\partial x_k) + R_{jk}\partial U_i/\partial x_k))$, hence it may be stated that the large scales due to the mean motion are responsible for creating turbulence anisotropy in wall-bounded flows. It may then be interesting to evaluate the eigenvalues of S_{ij} (say extensional, $S_\alpha > 0$, intermediate, S_β, and compressional, $S_\gamma < 0$), and project the flow statistics along the eigenvectors of S_{ij}. Evolution equations for the vorticity components in the local strain-rate eigenvector basis were given by Nomura and Post [25], applied to the case of homogeneous turbulence. Orlandi [26] exploited channel flow DNS at high Reynolds numbers [27–29], to evaluate the Reynolds stresses in the mean strain-rate eigenvector basis. In channel $S_\beta = 0$, hence one of the Reynolds stresses is unchanged, whereas the difference between the other two is reduced. The turbulence kinetic production in the mean strain-rate eigenvector basis is $P_k = -(P_\alpha + P_\beta + P_\gamma)$, with $P_\alpha = R_{\alpha\alpha}S_\alpha > 0$, and $P_\gamma = R_{\gamma\gamma}S_\gamma < 0$, larger than P_k in absolute value. In channels it was found that at any Reynolds number the compressive strain generates more kinetic energy than is destroyed by extensional one. These results may be useful to construct more reliable turbulence closures. For duct flows, it is difficult to get satisfactory results with models based on the linear eddy viscosity assumption [30]. Therefore the evaluation of the Reynolds stresses in the reference system based on the eigenvalues of S_{ij} may be of interest. A comparison between the

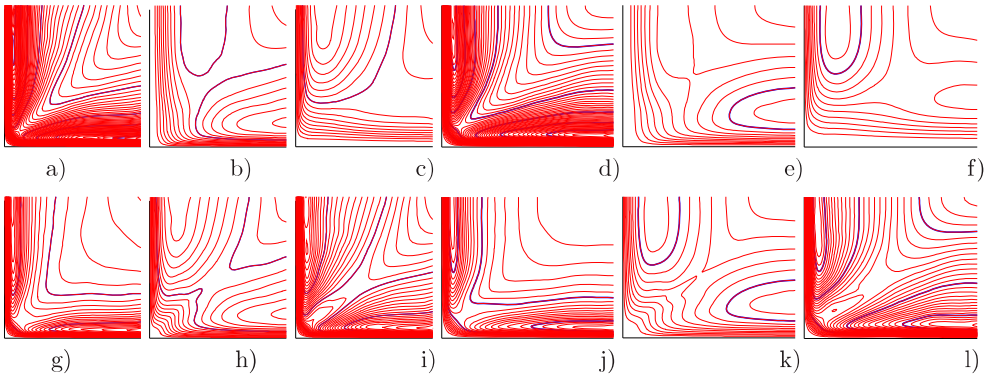

Figure 16. Contours of turbulent stresses in wall units at $Re = 7750$, in Cartesian basis (top), and in the mean strain-rate eigenvector basis (bottom); Red lines are spaced by $\Delta = 0.1$, and blue lines start from 1 and are spaced by $\Delta = 2$. (a) $R_{11}(6.28)$, (b) $R_{22}(1.52)$, (c) $R_{33}(1.67)$ for $A_R = 2$ (d) $R_{11}(5.6)$, (e) $R_{22}(1.15)$, (f) $R_{33}(1.16)$ for $A_R = 7$ (g) $R_{\alpha\alpha}(2.68)$, (h) $R_{\gamma\gamma}(3.90)$, (i) $R_{\beta\beta}(1.66)$ for $A_R = 2$, (j) $R_{\alpha\alpha}$ (2.39), (k) $R_{\gamma\gamma}(3.42)$, (l) $R_{\beta\beta}(1.16)$ for $A_R = 7$.

stresses in the Cartesian basis and those in the new basis is shown in Figure 16 at $Re = 7750$ for rectangular ducts with $A_R = 2$ and with $A_R = 7$. The contours for the square duct were shown in [22] by using a logarithmic scale for the distances from the corner to emphasise the near-wall behaviour. In all the cases, wall units are based on the mean friction velocity $\overline{u_\tau}$, that is also used to scale the normal stresses. The results at $Re = 7750$ may be regarded as representative of flows at high Reynolds number. A tendency towards an isotropisation and a symmetric distribution around the bisector was depicted in the new basis. In Figure 16, a linear scale for the coordinates, limited to a size of 200 wall units, is used. These plots, therefore allow to see the behaviour near the walls and in the outer region. The red contours are separated by $\Delta = 0.1$, blue contours starting from unit value, and separated by $\Delta = 1$ allow to emphasise the tendency towards an isotropisation in the mean strain-rate eigenvector basis, and to see whether a decrease of their level occurs by increasing the aspect ratio. To corroborate these occurrences, the maximum values are given in the caption. In the top figures, it is clear the strong stress anisotropy, and the high values at $A_R = 2$ with respect to those at $A_R = 7$. The anisotropy and the absence of any symmetry around the bisector make difficult their reproduction by RANS models. On the other hand, the bottom panels of Figure 16 show that turbulent stresses become symmetric with respect to the bisector in the mean strain-rate eigenvector basis also for $A_R = 7$. The anisotropy level is also reduced, in fact only the compressive stress in Figure 16(h,k) has two blue contours. As found by Orlandi [26] in two-dimensional channels, $R_{\gamma\gamma}$ is found to be larger than $R_{\alpha\alpha}$, leading to greater turbulence kinetic energy production through P_γ than the destruction by the extensional strain, P_α.

4. Concluding remarks

In this paper, we have reported results obtained from DNS of flow in rectangular ducts with different aspect ratios in the laminar, transitional and fully turbulent regimes. The

case of a square duct, largely investigated in real and numerical experiments has been preliminarily considered to validate the numerical method. The results compared well with those available in the literature. Particular attention has been directed to the time evolution towards a statistically steady state. We have found that the initial time units are necessary to destroy the unphysical flow structures related to the initial random disturbances. The analysis of the unsteady budget of the turbulence kinetic energy budget allows to understand the physics of wall turbulent flows. In fact, in the first period flow structures are generated in the entire duct, which are then convected by mean motion and transferred from one region to another by high-order velocity correlations, in addition to being produced and dissipated. Globally, the time variation of turbulence kinetic energy is associated with slight unbalance between production and dissipation. On the other hand, local variation of turbulence kinetic energy is strongly correlated with the local turbulent diffusion, with strong reduction of the turbulence kinetic energy in the central region of the duct at early times. At later times, kinetic energy is mainly produced near the walls and there locally dissipated, nevertheless large correlation between the local decay rate of turbulence kinetic energy and turbulent transport is still observed. This behaviour is typical of wall-bounded turbulent flows, and it corroborates the view that in turbulent flows local interaction is mainly driving the flow dynamics.

The wall profiles of τ_w increase starting from the corners, reaching a nearly flat distribution profile in a large part of the duct at sufficiently high Reynolds numbers. In addition, we have found that secondary motions are stronger at low than at high Reynolds number. Hence, at low *Re* secondary motions can be potentially exploited to improve mixing or heat transfer. At high *Re*, the reduction of the strength and the shrinking of the secondary motions to a small region near the corner yields a behaviour of C_f, as well to profiles of the mean motion and the turbulent statistics similar as in canonical two-dimensional channels. At high *Re*, there is no large difference on the definition of the reference length in plotting the C_f versus the bulk Reynolds number. On the other hand, in particular in the presence of rectangular ducts with $A_R > 1$, the transitional Reynolds number is independent of the aspect ratio by taking as reference length half of the shorter side. Having observed that for a square duct the critical *Re* is different from that for $A_R > 1$, we argue that for ducts with $A_R > 1$, asymmetric disturbances emanating from the corner act as a tripping device. At low *Re*, the shorter side plays an important role, and if the friction Reynolds number based on the short side is low, turbulence cannot be sustained and the flows remain laminar.

Scholars interested in applying RANS closures to simulate flows in practical applications for rectangular ducts are aware of the difficulties to reproduce anisotropy and asymmetries of the turbulent Reynolds stresses. In this paper, we have shown that by projecting the stresses along the mean strain eigenvectors, the anisotropy is reduced, and that the normal stresses become symmetric with respect the corner bisectors. This observation may be useful in constructing more reliable RANS closures. The further result that the behaviour of the total dissipation is simpler to model than the isotropic rate of turbulence kinetic energy could also be exploited in RANS closures.

In rectangular ducts at high Reynolds numbers, it has been found that the mean motion, the turbulence kinetic energy as well as its budget collapse well with the Reynolds number when expressed in wall units scale. These quantities also do not vary in the region near the corner as the aspect ratio is varied.

Acknowledgments

We acknowledge that some of the results reported in this paper have been achieved using the PRACE Research Infrastructure resource MARCONI based at CINECA, Casalecchio di Reno, Italy.

Disclosure statement

No potential conflict of interest was reported by the author(s).

References

[1] Vinuesa R, Noorani A, Lozano-Durán A, et al. Aspect ratio effects in turbulent duct flows studied through direct numerical simulation. J Turbul. 2014;15:677–706.
[2] Vinuesa R, Prus C, Schlatter P, et al. Convergence of numerical simulations of turbulent wall-bounded flows and mean cross-flow structure of rectangular ducts. Meccanica. 2016;51:3025–3042.
[3] Uhlmann M, Pinelli A, Kawahara G, et al. Marginally turbulent flow in a square duct. J Fluid Mech. 2007;588:153–162.
[4] Owolabi BE, Poole RJ, Dennisand DJC. Experiments on low-Reynolds-number turbulent flow through a square duct. J Fluid Mech. 2016;798:398–410.
[5] Faisst H, Eckhardt B. Sensitive dependence on initial conditions in transition to turbulence in pipe flow. J Fluid Mech. 2004;504:343–352.
[6] Carlson D, Widnall SE, Peeters MF. A flow-visualization study of transition in plane Poiseuille flow. J Fluid Mech. 1982;121:487.
[7] Orlandi P, Bernardini M, Pirozzoli S. Poiseuille and Couette flows in the transitional and fully turbulent regime. J Fluid Mech. 2015;770:424–441.
[8] Fitzgerald R. New experiments set the scale for the onset of turbulence in pipe flow. Phys Today. 2004;57:2.
[9] Hof B, Juel A, Mullin T. Scaling of the turbulence transition threshold in a pipe. Phys Rev Lett. 2003;91:244502.
[10] Reynolds O. On the dynamical theory of incompressible viscous fluids and the determination of the criterion. Phil Trans R Soc. 1895;186:123.
[11] Orlandi P. Time evolving simulations as a tentative reproduction of the Reynolds experiments on flow transition in circular pipes. Phys Fluids. 2008;20:101516.
[12] Tatsumi T, Yoshimura T. Stability of the laminar flow in a rectangular duct. J Fluid Mech. 1990;212:437.
[13] Takeishi K, Kawahara G, Wakabayashi H, et al. Localized turbulence structures in transitional rectangular-duct flow. J Fluid Mech. 2015;782:368–379.
[14] White FM. Viscous fluid flow. New York: McGraw-Hill; 1974.
[15] Gavrilakis S. Numerical simulation of low-Reynolds-number turbulent flow through a straight square duct. J Fluid Mech. 1992;244:101.
[16] Pirozzoli S, Modesti D, Orlandi P, et al. Turbulence and secondary motions in square duct flow. J Fluid Mech. 2018;840:631–655.
[17] Joung Y, Choi S, Choi J. Turbulence and secondary motions in square duct. J Eng Mech. 2007;133:213–221.
[18] Kim J, Moin P, Moser R. Turbulence statistics in fully developed channel flow at low Reynolds number. J Fluid Mech. 1987;177:133–166.
[19] Bernardini M, Pirozzoli S, Quadrio M, et al. Turbulent channel flow simulations in convecting reference frames. J Comput Phys. 2013;232:1–6.
[20] Orlandi P. Fluid flow phenomena: a numerical toolkit. Dordrecht: Springer Science & Business Media; 2012.
[21] Adams J, Swarztrauber P, Sweet R. Fishpack – A package of Fortran subprograms for the solution of separable elliptic partial differential equations; 1975. (NCAR Technical Note-TN/IA-109).

[22] Orlandi P, Pirozzoli S. DNS of transitional and turbulent flows in square ducts. J Turbul. 2020;21(2):106–128.
[23] Pope S. Turbulent flows. Cambridge: Cambridge University Press; 2000.
[24] Hartnett J, Koh JCY, McComas ST. A comparison of predicted and measured friction factors for turbulent flow through rectangular ducts. J Heat Trans TRANS ASME. 1962;84:82–88.
[25] Nomura K, Post GK. The structure and dynamics of vorticity and rate of strain in incompressible homogeneous turbulence. J Fluid Mech. 1998;377:65–97.
[26] Orlandi P. Turbulent kinetic energy production and flow structures in flows past smooth and rough wall. J Fluid Mech. 2019;866:897–928.
[27] Bernardini M, Pirozzoli S, Orlandi P. Velocity statistics in turbulent channel flow up to $Re_\tau = 4000$. J Fluid Mech. 2014;742:171–191.
[28] Lee M, Moser RD. Direct simulation of turbulent channel flow layer up to $Re_\tau = 5200$. J Fluid Mech. 2015;774:395–415.
[29] Yamamoto Y, Tsuji Y. Numerical evidence of logarithmic regions in channel flow at $Re_\tau = 8000$. Phys Rev Fluids. 2018;3:012062.
[30] Speziale C. On turbulent secondary flows in pipes of noncircular cross-section. Int J Eng Sci. 1982;20:863–872.